Proceedings of the ASME 2018
Dynamic Systems and Control Conference
DSCC2018
September 30-October 3, 2018, Atlanta, Georgia, USA

DSCC2018-9160

MODELING THE TRANSPORT DYNAMICS IN GASOLINE PARTICULATE FILTERS

Svyatoslav Korneev
Department of Energy Resources Engineering
Stanford University
Stanford, California 94305
Email: skorneev@stanford.edu

Simona Onori
Department of Energy Resources Engineering
Stanford University
Stanford, California 94305
Email: sonori@stanford.edu

ABSTRACT

We develop the flow and the particulate transport models in a wall-flow gasoline particulate filter (GPF). The filter is constituted of inlet channels which are separated from outlet channels by a porous wall. We model the flow inside the channel using incompressible Navier-Stokes equation coupled with the spatially averaged Navier-Stoke equation for the porous wall. For the particulate transport, we use coupled advection and spatially averaged advection-reaction equations, where the reaction term models the particles trapping. The concentration of deposited particulates at the back of the filter downstream the flow increases with Reynolds number. These results are in agreement with the published experimental measurements of the spatial distribution of particles inside the filter.

NOMENCLATURE

N_c number of channels in Gasoline Particulate Filter
D GPF diameter $[m]$
L GPF length $[m]$
h_w porous wall thickness $[m]$
h_w channel height $[m]$
h_w plug length $[m]$
l characteristic pore size $[m]$
$\hat{\mathbf{u}} = \{\hat{u}_x, \hat{u}_y\}$ flow velocity vector $[m/s]$
$\hat{t}$ time $[s]$
$\hat{\rho}$ fluid density $[kg/m^3]$
$\hat{p}$ pressure $[Pa]$
$\hat{\mathbf{x}} = \{\hat{x}, \hat{y}\}$ coordinate vector $[m]$
ν kinematic viscosity $[m^2/s]$
$\langle \hat{\mathbf{u}} \rangle$ filtration velocity $[m/s]$
$\langle \hat{p} \rangle$ macro-scale pressure $[Pa]$
$\hat{k}$ permeability $[m^2]$
u_{in} $\hat{x}$ component of the inlet flow velocity $[m/s]$
$\mathbf{u} = \{u_x, u_y\}$ flow velocity vector
$\mathbf{x} = \{x, y\}$ coordinate vector
t time
p pressure
Re Reynolds number
$\bar{\mathbf{u}}$ hybrid velocity
$\bar{\mathbf{p}}$ hybrid pressure
k permeability
α void/porous space indicator function
$\mathbf{n}$ normal vector
$\hat{c}$ particulate concentration $[kg/m^3]$
D particulate diffusion coefficient $[m^2/s]$
Pe_c Péclet number for the channel
c particulate concentration
c_{in} particulate concentration at the inlet
k_B Boltzmann's constant $[J/K]$
T fluid temperature $[K]$
r radius of particles $[m]$
Pe_c Péclet number for the porous wall
Da_c Damköhler number of the particles absorption
$\hat{a}$ rate of the particles absorption $[m/s]$
ε scales separation parameter
m power of the scales separation parameter
$D^\star$ dispersion tensor
u_w characteristic filtration velocity $[m/s]$
$\langle c \rangle$ macro-scale particulate concentration

$\hat{K}$ absorption rate $[1/s]$
K absorption rate
$\bar{c}$ hybrid concentration
Φ filtration efficiency
$U_{\text{filtration}}$ average velocity in the porous wall
U_{channel} average velocity in the central inlet channel
P_{inlet} average pressure at the inlet boundary

NOTATION

In this paper, the following notation is used:
$\mathscr{B}_l$ left boundary
$\mathscr{B}_r$ right boundary
$\mathscr{B}_t$ top boundary
$\mathscr{B}_t$ bottom boundary
$\mathscr{W}$ solid boundary
Ω_w porous sub-domain
Ω_v void sub-domain
$\cdot$ scalar product
$\nabla f(x,y) = \frac{\partial f}{\partial x}\bar{i} + \frac{\partial f}{\partial y}\bar{j}$ gradient along x,y directions
$\nabla \cdot \bar{F} = \frac{\partial F_x}{\partial x} + \frac{\partial F_y}{\partial y}$ divergence of vector field $\bar{F} = F_x\bar{i} + F_y\bar{j}$ along x,y directions
$\langle f \rangle$ volume averaging over the fluid phase

INTRODUCTION

To meet ever-more-rigorous fuel economy and emissions requirements, vehicle manufacturers are increasingly turning to Gasoline Direct Injection (GDI) engines. However, GDI engines result in higher particulate emissions due to shorter air/fuel mixing times, fuel impingement onto the piston, and other reasons [1].

Gasoline Particulate Filters (GPFs) have shown to be the most promising and practically adoptable solution in the near future. A wall-flow GPF consists of a monolithic structure with a bundle of axial parallel channels. Channels are alternatively plugged at each end (see Fig. 1(a) and Fig. 2) so that the gas in inlet channels is forced to flow across the porous wall of the GPF while particulate is removed from the exhaust gas [2, 3]. The accumulated particles reduce the filter permeability and create a high-pressure drop inside the exhaust system. The filter has to be periodically cleaned in order to maintain the optimal performance [4]. This procedure is known as GPF regeneration. The experimental measurements of particles concentration inside the porous wall show that the deposition process is non-uniform [5, 6].

Particles tend to accumulate predominantly at the back of the filter (see Fig. 1(c) for the nomenclature used for locations within the GPF).

Particulate present in the exhaust gas can be roughly divided into two categories. The first category is represented by soot.

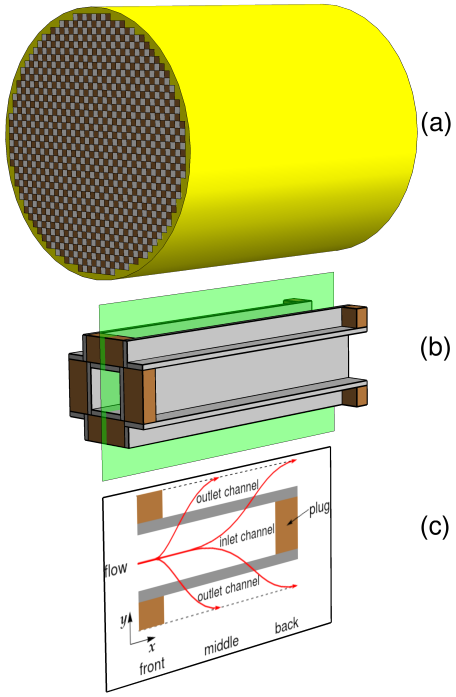

FIGURE 1: Schematic representation of (a) GPF, (b) 3D periodic "unit", (c) longitudinal cross-section of the 3D periodic "unit".

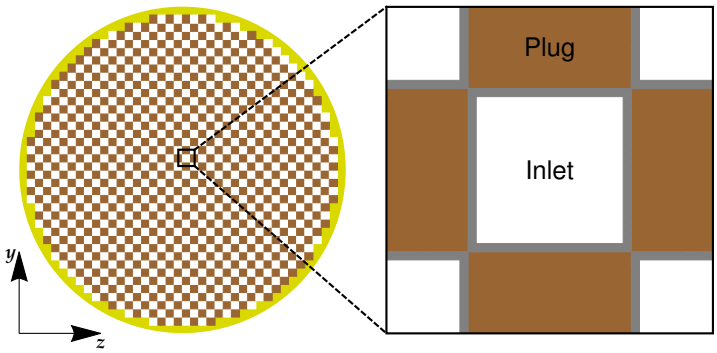

FIGURE 2: Top view of the GPF and a zoomed-in view of the periodic "unit". The yellow border corresponds to the filter monolith, the white small squares are the inlet channels and the brown ones are the plugs. Finally, the gray borders around the inlet channels and the plugs are the porous walls.

Soot particles may have a complex shape and constituted mainly of carbon [7]. The size distribution of the soot was measured experimentally [8]. The soot from the GDI engine is mostly made of nano-particles in the range 20-100nm. The second category is the ash flakes. Ash is made of hydrocarbon and oxides of various metals. The soot can be removed from the GPF by initiating the oxidation reaction, while the ash is not removable, and

Property	
Material	Cordierite
Diameter $\times$ Length	$D \times L = 118 \times 127\ (mm)$
Wall thickness	$h_w = 0.22\ (mm)$
Channel height	$h_c = 1.03\ (mm)$
Plug length	$l_p = 7\ (mm)$

TABLE 1: Geometric specifications of the Gasoline Particulate Filter.

60g of non-combustible material accumulates over 150,000mi of vehicle operation [9]. The regeneration can be performed by a passive means when the soot oxidation is initiated by the catalytic material dispersed on the surface of the porous wall, while in the active strategy, the oxidation is initiated by increasing the temperature of the exhaust gas entering the filter.

The filter dynamics includes the high velocity flow, thermal dynamics and particulate transport dynamics. The flow in the wall-flow filter was modeled in [10]. Authors showed that the suction velocity is non-uniform along the porous wall of the inlet channel and that this effect is more drastic when the flow velocity at the inlet is higher. The flow and the thermal dynamics in GPF were modeled in [11], but the particulate transport in GPF remains underrepresented in the literature.

We propose an accurate and reliable model for the fluid flow and the particulate transport in GPF. To verify the model, we numerically solve the flow and transport equations and analyze the spatial distribution of particles inside the porous wall. We show, that the predicted non-uniform distribution of the deposited particles is coherent with data published in [5, 6]. First, we simplify the GPF geometry using the quasiperiodicity of the GPF structure, second, we analyze the flow and transport equations for the void and the porous domains and finally, we couple equations across two domains. Using translational quasiperiodicity of GPF, we define the periodic "unit" to be the void central inlet channel which is separated from two outlet channels by the porous wall. For the flow and transport inside the void space, we use Navier-Stokes and advection equations. For the porous wall, we use spatially averaged equations since the characteristic pore size is a few magnitudes smaller than the length of the wall. For the flow, we use the spatially averaged Navier-Stokes equation with the momentum loss term, where the loss term accounts for the resistance of the porous wall. For the transport, we use the spatially averaged advection-reaction equation, where the reaction term accounts for the particulate trapping. The coupling of two Partial Differential Equations (PDEs) across different domains is a challenging problem [12]. We propose performing the coupling using the phase indicator function which is a simple and computationally efficient approach.

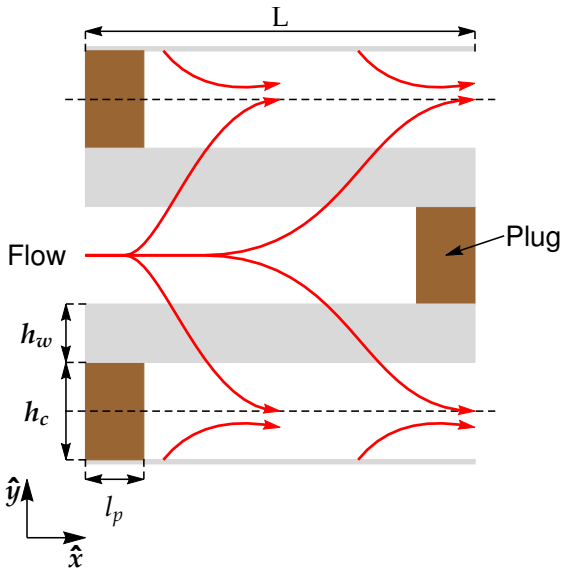

FIGURE 3: Schematic representation of the longitudinal cross-section, where the periodic "unit" is shown between horizontal dashed lines. Brown rectangles show the plugs, gray rectangles show the porous walls, and curved red arrows show the flow direction. The values of the geometric parameters are given in Table 1.

COMPUTATIONAL DOMAIN

In this paper, we consider the ceramic GPF with the characteristic pore size of $l = 10\mu m$. The GPF is built from a bundle of parallel squared channels of the same size (see Fig. 1(a)). The geometrical parameters of the channels are given in Table 1. The channels are alternately plugged at each front and back. The GPF top and the bottom views have a staggered pattern (see Fig. 2). The bundle of the staggered channels can be represented by the collection of spatially periodic "units". The periodicity breaks down at the filter boundary and the accuracy of the periodic representation scales as $\sim 1/\sqrt{N_c}$, where N_c is the total number of channels [13]. The flow and particulates are coming into the inlet channels, go through the porous wall and exits out of the outlet channels.

We model the dynamics in the longitudinal cross-section of the "unit" (see Fig. 3). Based on the geometry of the cross-section, we create the computational domain, where the model is evaluated (see Fig. 4). The domain consists of two sub-domains, Ω_v and Ω_w, respectively. The sub-domain Ω_v represents the void space of the central inlet and two outlet channels wherein the sub-domain Ω_w represents the porous wall. The domain has the inlet Boundary Conditions (BCs) at the left boundary ($\mathscr{B}_l$) and two outlets BCs at the right boundary ($\mathscr{B}_r$). The top ($\mathscr{B}_t$) and the bottom boundaries ($\mathscr{B}_b$) have periodic BCs. The solid black lines ($\mathscr{W}$) around the plugs represent the solid wall BCs.

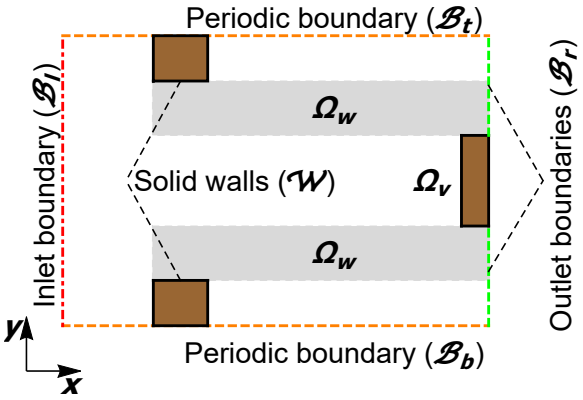

FIGURE 4: Schematic plot of the computational domain. The brown rectangles show the plugs. The red dot-dashed vertical lines show the inlet boundary ($\mathscr{B}_l$), the green vertical dashed lines show the outlet boundaries ($\mathscr{B}_r$), the orange horizontal dashed lines show the periodic boundaries ($\mathscr{B}_b$, $\mathscr{B}_t$). The black solid line framing the brown squares represent the solid wall (non-penetrable) boundaries ($\mathscr{W}$). The light gray rectangles show the porous sub-domain Ω_w and white area show the void space sub-domain Ω_v.

FLOW MODEL

We model the incompressible fluid flow across two spatially separated domains Ω_v and Ω_w. The flow inside sub-domain Ω_v is governed by Navier–Stokes equations

$$\begin{gathered}\frac{\partial \hat{\mathbf{u}}}{\partial \hat{t}}+\left(\hat{\mathbf{u}}\cdot\hat{\nabla}\right)\hat{\mathbf{u}}=-\frac{1}{\hat{\rho}}\hat{\nabla}\hat{p}+\nu\hat{\nabla}^2\hat{\mathbf{u}},\\ \nabla\cdot\hat{\mathbf{u}}=0,\ \hat{\mathbf{x}}\in\Omega_v,\end{gathered}\tag{1}$$

where $\hat{\mathbf{u}}$ is the flow velocity in the empty channel, $\hat{\rho}$ the fluid density, $\hat{p}$ pressure, ν kinematic viscosity, $\hat{\nabla}$ is the gradient operator and $\hat{\mathbf{x}}=\{\hat{x},\hat{y}\}$ is the 2D spatial coordinate. The compressibility effects are neglected since the flow velocity is order of magnitude smaller than the speed of sound.

We model the filtration velocity inside the porous wall Ω_w using the spatially averaged Navier-Stokes equation with the moment loss term which accounts for the resistance of the porous wall [14]

$$\begin{gathered}\frac{\partial\langle\hat{\mathbf{u}}\rangle}{\partial\hat{t}}+\left(\langle\hat{\mathbf{u}}\rangle\cdot\hat{\nabla}\right)\langle\hat{\mathbf{u}}\rangle=-\frac{1}{\hat{\rho}}\hat{\nabla}\langle\hat{p}\rangle+\nu\hat{\nabla}^2\langle\hat{\mathbf{u}}\rangle-\frac{\nu}{\hat{k}}\langle\hat{\mathbf{u}}\rangle,\\ \nabla\cdot\langle\hat{\mathbf{u}}\rangle=0,\ \hat{\mathbf{x}}\in\Omega_w,\end{gathered}\tag{2}$$

where $\hat{k}$ is the porous wall permeability, $\langle\hat{\mathbf{u}}\rangle$ is the average flow velocity in the porous wall or the filtration velocity and $\langle\cdot\rangle$ denotes to the volume averaging over the fluid phase in Representative Elementary Volume (REV). REV is the smallest part of the porous medium which includes all topological features. Non-local memory effects are neglected in Eq. 2. It is also assumed that the permeability does not change during the particulate deposition. The value of the permeability of the fresh filter was estimated in [6], $\hat{k}=1.9\mu m^2$.

Eqs. (1-2) are supported by the boundary conditions on the domains Ω_v, Ω_w interface and domains boundaries. Numerical coupling of two PDEs across different domains is a challenging problem. By introducing the dimensionless quantities

$$\begin{gathered}\mathbf{u}=\hat{\mathbf{u}}/u_{in},\ t=\hat{t}/\left(h_c/u_{in}\right),\\ \mathbf{x}=\hat{\mathbf{x}}/h_c,\ \ p=\hat{p}/\left(\rho u_{in}^2\right),\end{gathered}\tag{3}$$

where u_{in} is the horizontal component of the velocity at the domain inlet and h_c is the width of the inlet channel (see Tab. 1), Eqs. (1-2) are combined into the hybrid model

$$\begin{gathered}\frac{\partial\bar{\mathbf{u}}}{\partial t}+\left(\bar{\mathbf{u}}\cdot\nabla\right)\bar{\mathbf{u}}=-\nabla\bar{p}+\frac{1}{\mathrm{Re}}\nabla^2\bar{\mathbf{u}}-\frac{\alpha(\mathbf{x})}{\mathrm{Re}}\frac{1}{k}\bar{\mathbf{u}},\\ \nabla\cdot\bar{\mathbf{u}}=0,\ \mathbf{x}\in\Omega_c\cup\Omega_w\end{gathered}\tag{4}$$

where $\mathrm{Re}=u_{in}h_c/\nu$ is the Reynolds number and $\alpha(\mathbf{x})$ is the indicator function. Inside the void space $\mathbf{x}\in\Omega_v$, $\alpha=0$, and inside the porous wall $\mathbf{x}\in\Omega_w$, $\alpha=1$. The hybrid velocity $\bar{\mathbf{u}}$ models the flow in the empty channels $\mathbf{u}$ when $\alpha=0$ and the filtration velocity $\langle\mathbf{u}\rangle$ when $\alpha=1$. Eqs. (4) are supported by the boundary conditions

$$\begin{gathered}\bar{u}_x=1,\ \frac{\partial\bar{p}}{\partial x}=0,\ \mathbf{x}\in\mathscr{B}_l,\\ \bar{\mathbf{u}}=0,\ \mathbf{x}\in\mathscr{W},\\ \mathbf{n}\cdot\nabla\bar{\mathbf{u}}=0,\ \bar{p}=0,\ \mathbf{x}\in\mathscr{B}_r,\\ \bar{\mathbf{u}}(\mathbf{x})|_{\mathbf{x}\in\mathscr{B}_b}=\bar{\mathbf{u}}(\mathbf{x})|_{\mathbf{x}\in\mathscr{B}_t},\ \bar{p}(\mathbf{x})|_{\mathbf{x}\in\mathscr{B}_b}=\bar{p}(\mathbf{x})|_{\mathbf{x}\in\mathscr{B}_t}.\end{gathered}\tag{5}$$

where $\mathbf{n}$ is the normal to the surface vector and the boundaries ($\mathscr{B}_l$, $\mathscr{W}$, $\mathscr{B}_r$, $\mathscr{B}_t$ and $\mathscr{B}_b$) are shown in Figure 4.

PARTICULATE TRANSPORT MODEL

We model the particulate transport in the void sub-domain Ω_v using the advection-diffusion equation as follows

$$\begin{gathered}\frac{\partial\hat{c}}{\partial\hat{t}}=\hat{\nabla}\cdot\left(D\hat{\nabla}\hat{c}\right)-\hat{\nabla}\cdot\left(\hat{\mathbf{u}}\hat{c}\right),\\ \hat{\mathbf{x}}\in\Omega_v,\end{gathered}\tag{6}$$

where $\hat{c}$ is the particulate concentration per unit of volume, D the particulate diffusion coefficient and $\hat{\mathbf{u}}$ is the flow velocity defined by Eqs. (1). Rewriting Eq. (6) in terms of the dimensionless quantities (3) yields a dimensionless form of the transport equations

$$\begin{gathered}\frac{\partial c}{\partial t} = \frac{1}{\mathrm{Pe}_c}\nabla\cdot\nabla c - \nabla\cdot(\mathbf{u}c),\\ \mathbf{x}\in\Omega_v,\end{gathered} \tag{7}$$

where $\mathrm{Pe}_c = h_c u_{in}/D$ is Péclet number of the transport in the empty channel and the concentration is rescaled as $c = \hat{c}/c_{in}$, where c_{in} is the concentration at the domain inlet. To define the order of magnitude of the diffusion term in Eq. (7), we estimate the value of Pe_c. The characteristic value of particulate diffusion inside the fluid can be estimated by the Stokes–Einstein equation

$$D = \frac{k_B T}{6\pi\nu\rho r}, \tag{8}$$

where k_B is Boltzmann's constant, T the fluid temperature, and r the particle radius. The characteristic radius of the soot particle is $r = 50\mathrm{nm}$, the characteristic temperature of the fluid in the exhaust pipe is $T = 600\mathrm{K}$, the flow velocity is $u_{in} = 10m/s$, the kinematic viscosity of air is $\nu = 51.29\times10^{-6}m^2/s$ and the air density is $\rho = 0.59kg/m^3$. The estimated value of the Péclet number is $\mathrm{Pe}_c \sim 10^7$ which corresponds to the advection dominated transport regime. The diffusion can be neglected in Eq. (6) and the transport is governed by the advection equation

$$\begin{gathered}\frac{\partial c}{\partial t} = -\nabla\cdot(\mathbf{u}c),\\ \mathbf{x}\in\Omega_v.\end{gathered} \tag{9}$$

Analyzing the spatially averaged transport equation for the porous wall Ω_w is not straightforward, since the pore-scale flow contributes to the macro-scale dispersion [15, 16]. For the analysis we use the result of the asymptotic theory developed in [17]. The pore-scale transport in porous wall is governed by the dimensionless advection-diffusion equation with the Neumann boundary condition

$$\begin{gathered}\frac{\partial c}{\partial t} = \frac{1}{Pe_w}\nabla\cdot\nabla c - \nabla\cdot(\mathbf{u}c),\\ -\mathbf{n}\cdot\nabla c = \mathrm{Da}c,\end{gathered} \tag{10}$$

where the spatial coordinate is rescaled on the thickness of the porous wall $\mathbf{x} = \hat{\mathbf{x}}/h_w$, the velocity on the characteristic filtration velocity u_w, the Péclet number is $\mathrm{Pe}_w = h_w u_w/D$ and $\mathbf{n}$ is the vector normal to the surface of the porous wall. The boundary condition in Eq. (10) models the particulate absorption by the wall surface, where Damköhler number $\mathrm{Da} = h_w\hat{a}/D$ defines the ratio of the absorption and diffusion time scales where $\hat{a}$ is the rate of the particulate absorption [16]. Introducing the scales separation parameter ε, the transport equation can be written as [17]

$$\frac{\partial c}{\partial t} = \varepsilon^m\nabla\cdot\nabla c - \nabla\cdot(\mathbf{u}c), \tag{11}$$

where ε is the scale separation parameter which is defined by the ratio of the pore- and macro-length-scales $\varepsilon = l/h_w$. When the power of the ε is greater than 2, the dispersion term can be neglected in averaged equation $D^\star\nabla\cdot\nabla\langle c\rangle \sim 0$, where $D^\star$ is the dispersion tensor [15, 16]. In this work we estimate the values of m and ε for the GPF. The characteristic pore size of the cordierite porous wall is $l = 10\mu m = 10^{-5}m$ and the scales separation parameter is equal to $\varepsilon = 0.0454$. The estimated filtration velocity u_w is approximately 100 times less than the velocity in the inlet channel (see Tab. 2). Given the inlet velocity is $10m/s$, the characteristic filtration velocity turns out to be $u_w = 0.1m/s$. The Péclet number for the porous wall is $\mathrm{Pe}_w = 5.43\times10^4$ and the power of ε is equal to $m = -\log(\mathrm{Pe}_w)/\log(\varepsilon) = 3.52$.

The dispersion for the macro-scale transport can be neglected and the transport inside the porous wall is governed by the advection-reaction equation. In terms of the dimensionless quantities (6) the averaged transport equation takes the form

$$\begin{gathered}\frac{\partial\langle c\rangle}{\partial t} = -\nabla\cdot(\langle\mathbf{u}\rangle\langle c\rangle) - K\langle c\rangle,\\ \mathbf{x}\in\Omega_w.\end{gathered} \tag{12}$$

where the absorption rate and the concentration are rescaled as $K = \hat{K}/(u_{in}/h_c)$, $c = \hat{c}/c_{in}$, and $\langle\mathbf{u}\rangle$ is the dimensionless filtration velocity. This type of equation is well-known in modeling of the colloids transport in porous medium [18]. To estimate K, one have to perform the breakthrough experiment [18] with GPF and particles of given size. To our best knowledge the breakthrough experimental data for GPF is not published and we estimate K in order to have the filtration efficiency (please see Eq. 15) between $0.6-0.9$ [9].

Using the indicator function $\alpha(\mathbf{x})$, we combine Eqs. (9) and (12) into the single hybrid equation

$$\begin{gathered}\frac{\partial\bar{c}}{\partial t} = -\nabla\cdot(\bar{\mathbf{u}}\bar{c}) - \alpha K\bar{c},\\ \mathbf{x}\in\Omega_c\cup\Omega_w\end{gathered} \tag{13}$$

where $\bar{\mathbf{u}}$ is governed by Eq. (4). Eq. (13) is supported by the boundary conditions

$$\begin{gathered} \bar{c} = 1, \ \mathbf{x} \in \mathscr{B}_l, \\ \mathbf{n} \cdot \nabla \bar{c} = 0, \ \mathbf{x} \in \mathscr{W}, \\ \frac{\partial \bar{c}}{\partial x} = 0, \ \ \mathbf{x} \in \mathscr{B}_r, \\ \bar{c}\,(\mathbf{x})\,|_{\mathbf{x} \in \mathscr{B}_b} = \bar{c}\,(\mathbf{x})\,|_{\mathbf{x} \in \mathscr{B}_t}. \end{gathered} \tag{14}$$

The filtration efficiency is defined by the ratio of particulate fluxes at the inlet and outlets as follows

$$\Phi = 1 - \left(\int_{\mathscr{B}_r} \bar{u}_x \bar{c} dx \right) / \left(\int_{\mathscr{B}_l} dx \right), \tag{15}$$

where $\bar{u}_x$ is the x component of the flow velocity and inlet dimensionless flow velocity and the concentration is equal to 1.

NUMERICAL RESULTS

To verify the proposed model, we numerically solve the flow (4) and the transport (13) equations with the boundary conditions (5) and (14). We use Finite-Volume framework available in the Open source Field Operation And Manipulation (OpenFOAM) software. OpenFOAM is a C++ toolbox for the development of customized numerical solvers and solution of continuum mechanics problems, including computational fluid dynamics. OpenFOAM includes the mesh utilities, customizable solvers of PDE and utilities for the post-processing. We create the solver for the hybrid flow equation by modifying the large time-step transient solver for incompressible flow *pimpleFOAM*. For the solution of the hybrid transport equation, we modified the advection-diffusion solver *transportFOAM*.

We create the Cartesian computational mesh using utility *blockMesh*. The mesh lower-right point has coordinates $(x,y) = (-10,-1.2135)$ and the upper-right point $(x,y) = (119.9029, 1.2135)$. The x coordinate of the central inlet is 0. The mesh has 5252 cells along the x direction and 100 cells along the y direction. Using utility *snappyHexMesh*, we cut the plugs from the mesh. For the mesh preparation, we use the standard set of parameters [19].

We run the flow simulations using three values of Reynolds number $\mathrm{Re} = \{50, 250, 500\}$. The characteristic values of Re proper for the vehicle gas exhaust system were estimated based on the lowest/highest values of the mass flow rate and the exhaust temperature from [20] and the diameter of GPF from Table 1. The values of Re were also estimated in [11]. The results of the flow simulations are shown in Figures 5 and 6. We rescaled the width of all figures on 0.1. The simulations of the flow and transport equations converge to the steady-state solution with accuracy 10^{-5}.

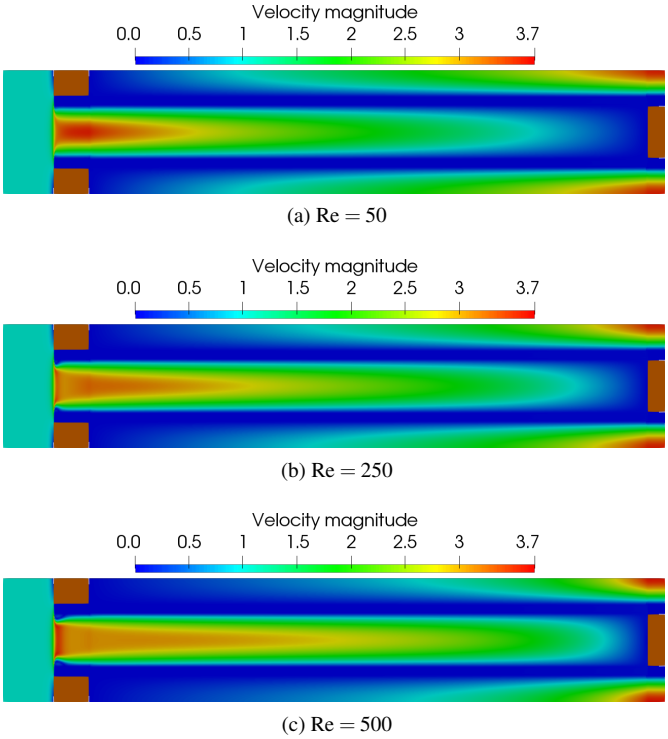

(a) $\mathrm{Re} = 50$

(b) $\mathrm{Re} = 250$

(c) $\mathrm{Re} = 500$

FIGURE 5: Steady-state distribution of the flow velocity magnitude for $\mathrm{Re} = \{50, 250, 500\}$. Brown rectangles show the location of the plugs. The width of the figures is rescaled on 0.10.

The stream-lines plot in Fig. 6 shows the direction of the fluid flow. The streamlines are noticeably denser at the back of the inlet channel. Since the flow intertia dominates, this effect of nonuniform flow increases with higher Re. The streamlines plot also shows the path of the particulate transport in the advective transport regime. Particulate is enforced to pass through the porous wall at the back of the channel, which is in agreement with the experimental measurements of the particles distribution inside the porous wall [5, 6]. The steady-state solution are asymmetric, despite the domain and the boundary conditions are symmetric. The breaking of the flow symmetry in a channel with sudden contraction/expansion was recently investigated numerically and experimentally [21]. The steady-state particulate concentration is shown in Figure 7. The particulate transport through the porous wall is localized at the back of the channel for the hight Re.

CONCLUSIONS

We propose a hybrid model of the particulate transport in GPF. The model accounts multi-scale feature of the GPF geom-

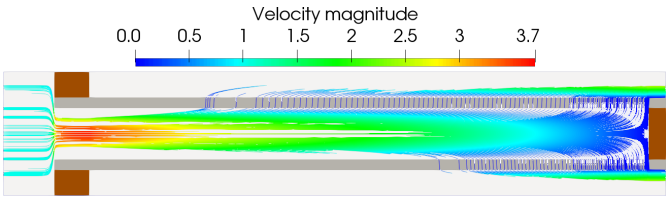

(a) Re = 50

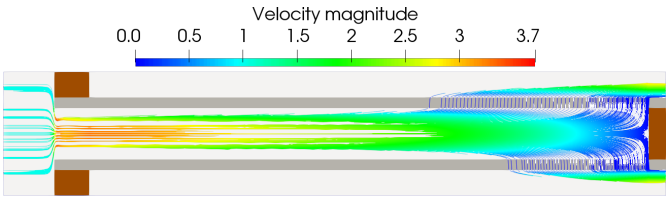

(b) Re = 250

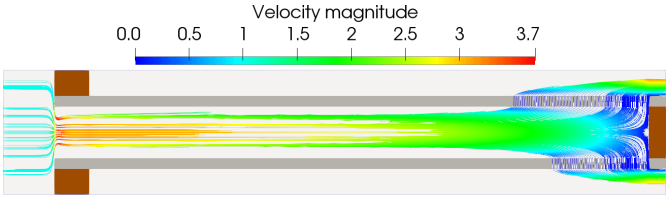

(c) Re = 500

FIGURE 6: The stream-lines plot of the steady-state flow for $\mathrm{Re} = \{50, 250, 500\}$, where color of the stream-lines corresponds to the velocity magnitude. The dark gray regions show the location of the porous walls whereas the brown rectangles indicate the plugs location. The width of the figures is rescaled on 0.10.

	Re = 50	Re = 250	Re = 500
$U_{\text{filtration}}$	9.3×10^{-3}	9.5×10^{-3}	9.5×10^{-3}
U_{channel}	1.312	1.435	1.634
P_{inlet}	69.988	18.816	12.864

TABLE 2: Characteristic parameters of the flow from the numerical solution of (4), where $\mathscr{U}_{\text{filtration}}$ is the average velocity in the porous wall, $\mathscr{U}_{\text{channel}}$ in the central inlet channel and $\mathscr{P}_{\text{inlet}}$ the average pressure at the inlet boundary.

etry by coupling the detailed equations for the empty channel with the averaged equations for the porous wall. The coupling was performed using a very simple approach, which requires a minimum modification of the existing numerical CFD solvers. The simulations show that the proposed model captures the non-uniform distribution of the particulate deposition. This result is consistent with the data reported in the literature. The model can be extended to the case when the permeability of the porous wall changes during the particulate deposition and the soot regeneration.

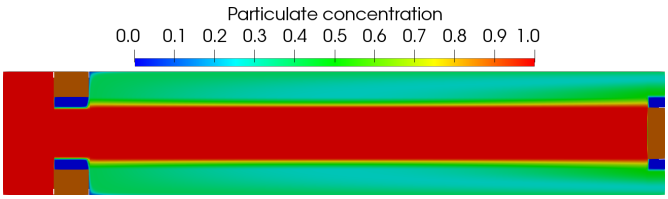

(a) Re = 50

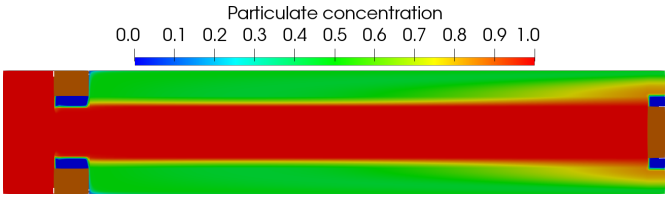

(b) Re = 250

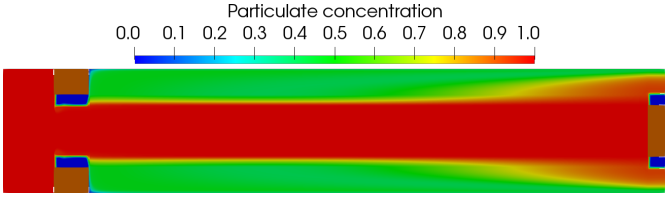

(c) Re = 500

FIGURE 7: Steady-state particulates concentration distribution for $\mathrm{Re} = \{50, 250, 500\}$. Brown shows the location of the plugs. The width of the figures is rescaled on 0.10.

ACKNOWLEDGMENT

This material is based upon work supported by the National Science Foundation under grant No. CAREER CMMI 1653836.

REFERENCES

[1] Maricq, M. M., and Xu, N., 2004. "The effective density and fractal dimension of soot particles from premixed flames and motor vehicle exhaust". *Journal of Aerosol Science,* ***35***(10), pp. 1251–1274.

[2] Konstantas, G., and Stamatelos, A., 2004. "Computer aided engineering of diesel filter systems". In Joint Meeting of the Italian and the Greek Section of the Combustion Institute, pp. 17–19.

[3] Thompson, G. J., Carder, D. K., Besch, M. C., Thiruvengadam, A., and Kappana, H., 2014. "In-use emissions testing of light-duty diesel vehicles in the united states". *Retrieved from the International Council on Clean Transportation website http://www. theicct. org/sites/default/files/publications/WVU_LDDV_ in-use_ICCT_Report_Final_may2014. pdf.*

[4] Chan, T. W., Saffaripour, M., Liu, F., Hendren, J., Thomson, K. A., Kubsh, J., Brezny, R., and Rideout, G., 2016.

"Characterization of Real-Time Particle Emissions from a Gasoline Direct Injection Vehicle Equipped with a Catalyzed Gasoline Particulate Filter During Filter Regeneration". *Emission Control Science and Technology,* ***2***(2), pp. 75–88.

[5] Lambert, C. K., Chanko, T., Jagner, M., Hangas, J., Liu, X., Pakko, J., and Kamp, C. J., 2017. "Analysis of Ash in Low Mileage, Rapid Aged, and High Mileage Gasoline Exhaust Particle Filters". *SAE International Journal of Engines,* ***10***(4), pp. 2017–01–0930.

[6] Lambert, C. K., Bumbaroska, M., Dobson, D., Hangas, J., Pakko, J., and Tennison, P., 2016. "Analysis of High Mileage Gasoline Exhaust Particle Filters". *SAE International Journal of Engines,* ***9***(2), pp. 2016–01–0941.

[7] Stanmore, B. R., Brilhac, J. F., and Gilot, P., 2001. "The oxidation of soot: A review of experiments, mechanisms and models". *Carbon,* ***39***(15), pp. 2247–2268.

[8] Eastwood, P., 2008. *Particulate emissions from vehicles*, Vol. 20. John Wiley & Sons.

[9] Lambert, C., Chanko, T., Dobson, D., Liu, X., and Pakko, J., 2017. "Gasoline Particle Filter Development". *Emission Control Science and Technology,* ***3***(1), pp. 105–111.

[10] Oxarango, L., Schmitz, P., and Quintard, M., 2004. "Laminar flow in channels with wall suction or injection: A new model to study multi-channel filtration systems". *Chemical Engineering Science,* ***59***(5), pp. 1039–1051.

[11] Pozzato, G., Hoffman, M. A., and Onori, S., 2017. "Multichannel physics-based modeling and experimental validation of an uncoated Gasoline Particulate Filter in clean operating conditions". In 2017 American Control Conference (ACC), IEEE, pp. 5392–5397.

[12] Battiato, I., Tartakovsky, D. M., Tartakovsky, A. M., and Scheibe, T. D., 2011. "Hybrid models of reactive transport in porous and fractured media". *Advances in Water Resources,* ***34***(9), pp. 1140–1150.

[13] Korneev, S., and Battiato, I., 2016. "Sequential Homogenization of Reactive Transport in Polydisperse Porous Media". *Multiscale Modeling & Simulation,* ***14***(4), jan, pp. 1301–1318.

[14] Hamdan, M., and Barron, R., 1991. "Analysis of the darcy-lapwood and the darcy-lapwood-brinkman models: significance of the laplacian". *Applied Mathematics and Computation,* ***44***(2), pp. 121 – 141.

[15] Auriault, J.-L., and Adler, P., 1995. "Taylor dispersion in porous media: analysis by multiple scale expansions". *Advances in Water Resources,* ***18***(4), pp. 217–226.

[16] Battiato, I., and Tartakovsky, D., 2011. "Applicability regimes for macroscopic models of reactive transport in porous media". *Journal of contaminant hydrology,* ***120***, pp. 18–26.

[17] Hou, T. Y., and Liang, D., 2009. "Multiscale analysis for convection dominated transport equations". *Discrete and Continuous Dynamical Systems,* ***23***(1-2), pp. 281–298.

[18] Kretzschmar, R., Barmettler, K., Grolimund, D., Yan, Y.-d., Borkovec, M., and Sticher, H., 1997. "Experimental determination of colloid deposition rates and collision ef ciencies in natural porous media". *Water Resources,* ***33***(5), pp. 1129 –1137.

[19] "http://cfd.direct/openfoam/user-guide/snappyhexmesh/".

[20] Galindo, J., Serrano, J., Dolz, V., and Kleut, P., 2015. "Brayton cycle for internal combustion engine exhaust gas waste heat recovery". *Advances in Mechanical Engineering,* ***7***(6).

[21] Mizushima, J., and Shiotani, Y., 2000. "Structural instability of the bifurcation diagram for two-dimensional flow in a channel with a sudden expansion". *Journal of Fluid Mechanics,* ***420***, pp. 131–145.